A method for identification of an effective Winkler foundation for largediameter offshore wind turbine support structures based on in-situ measured small-strain soil response and 3D modelling

Versteijlen, Pim; Metrikine, Andrei; van Dalen, Karel

DOI
10.1016/j.engstruct.2016.06.007

Publication date
2016

Document Version
Accepted author manuscript

Published in
Engineering Structures

A method for identification of an effective Winkler foundation for large-diameter offshore wind turbine support structures based on in-situ measured small-strain soil response and 3D modelling

W.G. Versteijlen[a,b], A.V. Metrikine[b], K.N. van Dalen[b]

[a]*Siemens Wind Power, Beatrixlaan 800, 2595 BN Den Haag, The Netherlands*
[b]*Faculty of Civil Engineering and Geosciences, Delft University of Technology, Stevinweg 1, 2628CN Delft, The Netherlands*

Abstract

A procedure is presented for the derivation of an effective small-strain soil stiffness governing the soil-structure interaction of large-diameter monopiles. As a first step, geophysical measurements are used to estimate the depth-dependent shear modulus G of the soil stratum. The second step is to use this modulus and an estimated Poisson's ratio and density in a 3D model, which captures the deformation of both the monopile and the soil. As a final step, a new method is proposed to use the computed 3D response for identification of a depth dependent stiffness of an effective Winkler foundation. This stiffness can be used in a 1D model, which is more fit for design purposes. The presented procedure is deemed more appropriate than the often used "p-y curve" method, which was once calibrated for slender flexible piles and for which the input is based on the large-strain cone penetration test. The three steps are demonstrated for a particular design location. It is also shown that the displacements of the 3D model are smaller and the resulting fundamental natural frequency is higher than calculated with the p-y method.

Keywords: offshore wind foundations, fundamental natural frequency, small-strain soil stiffness, in-situ seismic measurement, 3D to 1D modelling translation

1. Introduction

The interaction of the large diameter foundations of offshore wind turbines (OWTs) with the surrounding soil is one of the key research areas in which the offshore wind industry expects to cut conservatism in design. The most popular "monopile" (MP) foundation is thought to be over-designed, mainly due to a lack of knowledge of both the effective soil stiffness and damping governing the inclination and bending of MPs that reach up to 10m diameter in current designs [1].

When the fundamental natural frequencies of installed OWTs are monitored, a quite consistent discrepancy is found between this measured frequency and the design-aimed frequency; up to 20% higher frequencies are measured, with most turbines within the 5% higher range [1]. This frequency corresponds to the first bending mode of the support structure (MP + turbine tower). Due to the symmetry of an MP-based OWT, the structure has in fact 2 closely spaced first bending modes, vibrating in perpendicular directions: the fore-aft bending mode (F-A) and the side-side mode (Si-Si). The frequencies of these modes are key design parameters, as they need to be placed outside the resonance regimes of the wind and wave loads and the blade-passing frequencies. The fact that

the true frequency is often higher than the one designed for is expected to be caused by underestimation of the soil stiffness. The over-dimensioning of the support structure is mainly a waste of steel as often larger diameter foundation piles are employed to reach the desired fundamental natural frequency. It also involves a risk that the higher natural frequency enters another resonance region. For some design locations, however, it might result in a longer life-time, as less amplification of the low-frequency wave loading takes place. In any case, a correct prediction of the fundamental frequency is desirable.

The engineering approach for modelling the stiffness between the soil and the MP is called the "p-y curve" method, prescribed in the design standards [2]. In this approach, the pile is modeled as an Euler-Bernoulli beam, laterally supported by uncoupled discrete non-linear springs. The displacement-dependent stiffness of these springs is based on semi-empirical relations found for slender, small-diameter piles in both clay [3] and sand [4]. The initial stiffness of these springs that corresponds to small strains, has a large effect on the natural frequency of the OWT as it is this small-strain stiffness that defines the modal properties of the support structure. Furthermore, the soil response is expected to be linear for most of the endured vibrational amplitudes during the lifetime

of the foundation [5]. This initial part of the stiffness k_s [N/m^2] [1] is often called the initial subgrade modulus $k_{s,0}$ or E^*_{py}. In the *p-y* curve formulation for sand, k_s is calculated by multiplying k, the modulus of subgrade reaction [N/m^3] (first described by Terzaghi [6]), with depth z. k is only determined with the angle of internal friction of sand ϕ. Note that this k is a true soil-structure interaction (SSI) modulus; it was once calibrated on the way slender piles react when embedded in specific soil types.

It is widely accepted that different physical mechanisms play a role in the SSI depending on the geometry of the pile [7], [8], [9] and [10]. The ratio of embedded length L and diameter D (L/D) of the MPs that are currently employed in the industry, is expected to invoke a fundamentally different soil reaction than what the *p-y* curves were originally calibrated for [11]. For instance, this design method does not account for large shearing contributions of the pile-tip [12], in-plane deformation of the pile and soil stiffening due to vertical interaction of the soil layers. The currently used monopiles are significantly stiffer in bending than the flexible piles for which the *p-y* curves are supposed to be used. The *p-y* curve method was developed for defining the stiffness of the Winkler foundation

[1] The stiffness k_s is computed per unit vertical length of the pile, explaining the dimension [N/m/m].

model. In this model, the foundation reaction is completely local: the reaction force is only dependent on the displacement of the pile at the location of that spring. For a flexible pile, this is not a bad assumption. However, deflections of rigid, caisson-type piles, evoke more global reactions of the soil. Apart from this, it is incorrect to assume that the initial stiffness of the effective springs is independent of the geometry of the pile. Furthermore, the assumption that this stiffness would increase linearly with depth for any type of sand, is expected to be incorrect [13]. Because of these shortcomings and because of its relevance, the initial stiffness has already been critically studied by several researchers [8], [14], [15]. Seemingly contradictory to what is measured in the field, it was found in these studies that the p-y curve method actually over-predicts the initial stiffness of the soil for larger depths. If this were generally the case, it would not explain the higher natural frequencies that are measured. Alternatively, it might indicate that the shallow depth soil reaction is mostly responsible for the higher measured natural frequency. The researchers therefore suggest that a more realistic variation - taking 3D, global effects into account - of the stiffness with depth might rather follow a power law form with an exponent smaller than 1 [13]. As the stiffness depends on the soil type, the geometry of the structure, and the loading type, it remains challenging to find a general solution method

for this problem. Depending on the focus of the researchers, and possibly the applied advanced modelling techniques, different methods are suggested. In geotechnical design, empirical tuning factors are often used to capture the complex interaction of the soil with different structure types. For instance, in the OWT-related research, large diameter-effect tuning factors were suggested to improve initial stiffness predictions [8], [9] and [10]. Recently however, some of these suggested p-y relations were said to be incorrect or at least not generally applicable, and a new method was presented [16].

Apart from modelling aspects, the methods used for soil characterization in the wind industry can also be improved. The most applied soil measurements in the OWT industry are geotechnical tests like the cone penetration tests (CPT) and laboratory testing of borehole samples. It is clear that these techniques are soil-disturbing, large-strain measurements, and one may question whether they allow to assess the small-strain behaviour of the soil.

Clearly, we need to find the characteristics dictating the response of the foundation. Therefore, as in [17], an approach including geophysical (seismic) measurements is suggested in this paper. While the CPT measures local resistance and friction along the shaft, a recorded wave in the soil carries information about

the soil characteristics on the wave-length scale (in the order of several meters), yielding more global effective parameters for a certain location. By measuring the wave velocities in-situ, all local properties (like oedometric stiffening and saturation effects) are incorporated. This can be considered as an advantage over most laboratory tests in which these in-situ characteristics are partially lost.

Focusing on initial stiffness modelling, this paper suggests an approach in which a 3D model is used to calibrate the initial part of the p-y curves. The model incorporates 3D soil effects and shell deformations of the pile. The novelty of the approach lies in using in-situ seismic measurements to extract the small-strain shear modulus (described in Section 2) and - instead of using the continuum parameters in a general empirical relation for the 1D stiffness as is done in [18] and in [19] - the continuum parameters are used to define a 3D model to compute pile deflection shapes for a certain loading (Section 3). Subsequently, a general translation method is suggested for finding the 1D effective stiffness (i.e., the initial branch of the p-y curve) from the numerically computed 3D response (Section 4). As many parameters influence the true SSI, we suggest using the presented translation method at the start of each design effort, rather than finding one empirical tuneable relation. In this translation, we constrain ourselves

by only considering lateral springs, and we exclude other elements such as rotational springs, as was done in [20]. However, when considering these large foundations, introducing rotational springs in the 1D model can be justified. Rotational springs can physically be understood to represent the distributed bending moment that is induced by the vertical shearing forces on the pile wall that, due to the rigid behavior have a more uniform direction and due to the large diameter, work at a greater lever arm. Nevertheless, in order to serve the current wind design practice, a 1D effective model with only translational springs will be presented in this paper.

2. Soil characterization

An extensive in-situ soil measurement campaign was carried out by a geotechnical service company for the design of a near-shore wind farm. Besides the standard geotechnical measurements (CPT and lab tests on borehole samples), seismic cone penetration tests (SCPTs) were also performed at some locations. In this section, we describe a method for analyzing this data. In this characterization, we assume that small vibrations of the soil can be described by the classical elastic continuum with frequency-independent parameters.

We analyzed seismic data of a location close to one of the design locations.

The SCPT reached a depth of 25m at this location, measuring each meter with a dual-phone cone with an interval distance of 0.5m. A hydraulic shear-wave hammer placed on the seabed was used as excitation device. Stacking responses over multiple hits for each depth rendered clear shear-wave patterns. The seismogram of the recorded time traces is shown in Figure 1.

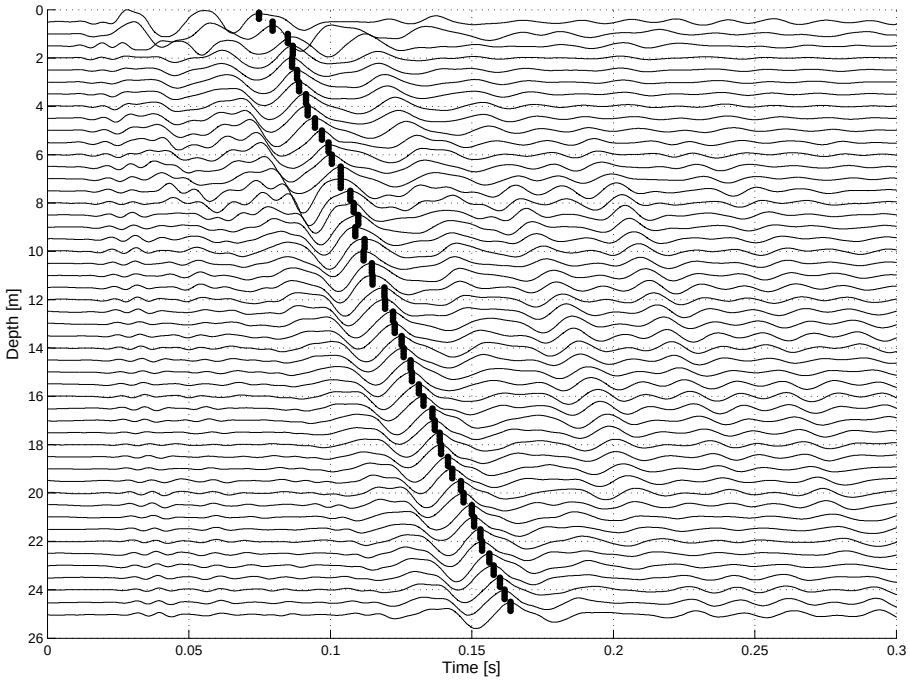

Figure 1: Seismogram showing the time traces of the particle velocities in horizontal direction (in-line with the shear-wave hammer) measured at each geophone. The picked arrival times are indicated at each time trace with black dots.

We will now firstly discuss how the arrival time of the measured waves was defined (Section 2.1), as this choice influences the magnitude of the shear-wave

velocity that will subsequently be determined. In Section 2.2, a simple model is used to invert the seismic data in order to find the shear-wave velocities based on the identified interval times of Section 2.1. In Section 2.3 all other parameters are listed that are needed to describe the soil continuum. Then 3 different stiffness profiles are defined in Section 2.4, as some parameters have some variability depending on choices made in the interpretation. Finally, Section 2.5 compares the determined shear modulus profile with an often used empirical relation between shear modulus and CPT output.

2.1. Wave arrival timing

To determine the shear-wave velocity, we need to know the path length of the wavefront, and define its arrival time at the measuring sensor, the geophone. Different definitions of this "arrival time" exist. We defined the moment of appearance of the maximum particle velocity of the soil as the arrival time of the wavefront, as this allows for automated picking. The picked arrival times are indicated with black dots in Figure 1. Nevertheless, these "picks" have to be visually checked, as the waveform needs to be consistent. Especially in the first few meters, the waveform tends to change significantly in the course of propagation due to near-field (near to source) effects. Hence, for the first 4 traces belonging to the first 2m below the seabed, different peaks were picked

manually, to give consistent interval times.

The difference in arrival time between two adjacent receivers - the interval time - can be obtained by subtracting the arrival time of the upper geophone from that of the lower geophone. The interval time between the geophones can also be obtained by cross correlation, which is a more objective technique. The interval times found by both picking and cross correlation are displayed in Figure 2. We observe that cross correlation gives more smooth results, especially for depths between 7 to 13m. As the near-field effects within the first 2m seem to make the use of cross correlation less reliable, a time-frequency analysis was used to pick the maximum energy peak, as shown in Figure 3. The time-frequency analysis was done using the S-transform [21]. The S-transform showed that the region of maximum energy in the spectrum of the recording at 2m depth was shifted in frequency content with regards to those at 0.5m, 1m and 1.5m depth. Altogether, the wave arrival for the first 2 meters remains uncertain, but more consistent results are found for larger depths. A smoother profile is expected to be more realistic, as we expect the soil to be smoothly inhomogeneous. As we will show in Section 2.4, the variability in the interval times for these shallow layers do have a significant effect on the stiffness estimation of the upper half

of the stratum. In the next section, the corresponding shear-wave velocities of these interval-time profiles will be computed, and a choice will be made as to which profile is deemed to be most realistic.

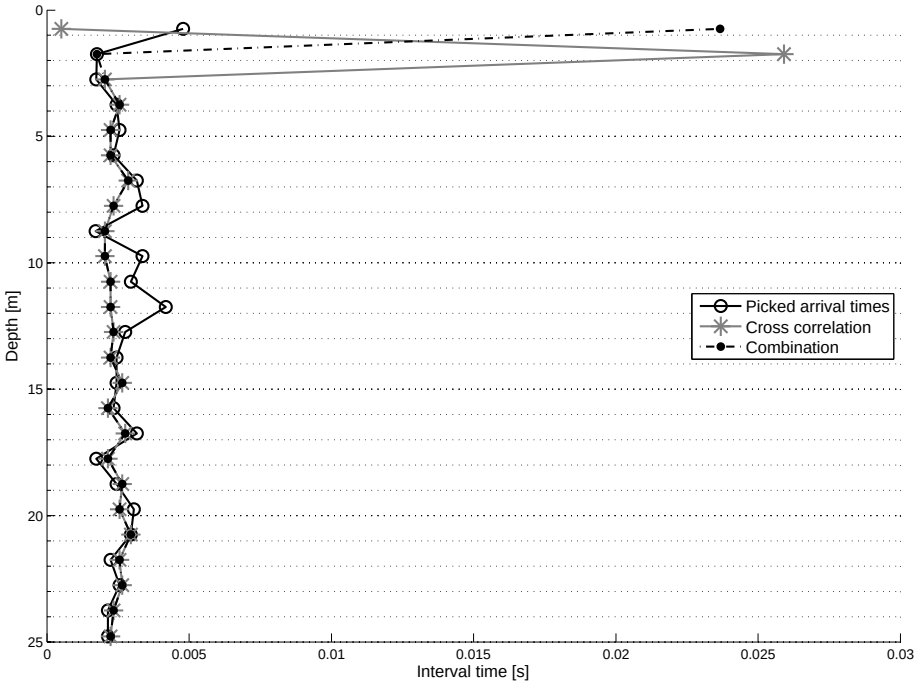

Figure 2: Interval times between adjacent geophones. The interval times can be defined as the difference in picked arrival times (black "o"), or determined with cross correlation (grey "∗"). A combination can also be chosen (black "•"); cross correlation was used for all interval times except for the first layer, where the S-transform technique was used, and the second layer, which was manually picked (see Section 2.2).

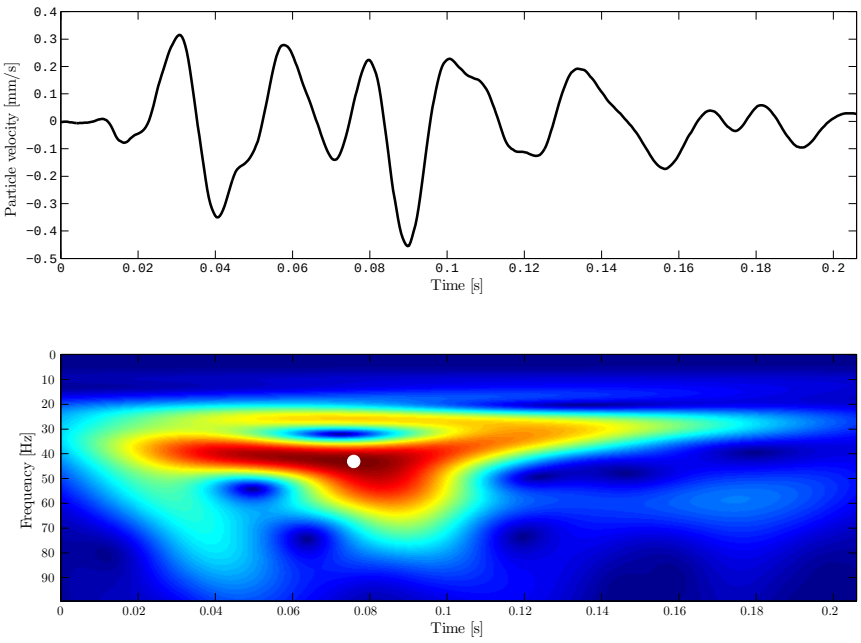

Figure 3: Time response of the geophone placed at 1m depth (upper panel), and the corresponding time-frequency diagram (lower panel). The maximum energy is indicated with a white dot.

2.2. Shear-wave velocity inversion

To find the shear-wave velocities, a minimization problem was set up. Assuming the soil to be horizontally stratified with a layer thickness of 1m around a geophone pair of one stacked recording, the successive layer shear-wave velocities can be computed by minimizing an objective function for the observed arrival times. The method incorporates the effect of wave refraction through Snell's law, which has to be taken into account because of the horizontal offset between the source and the receivers. Especially for shallower layers, this effect cannot

be ignored.

The geometry of the minimization problem is shown in Figure 4, in which an example is given for layer number $n = 3$. The equations of the optimization problem are given by

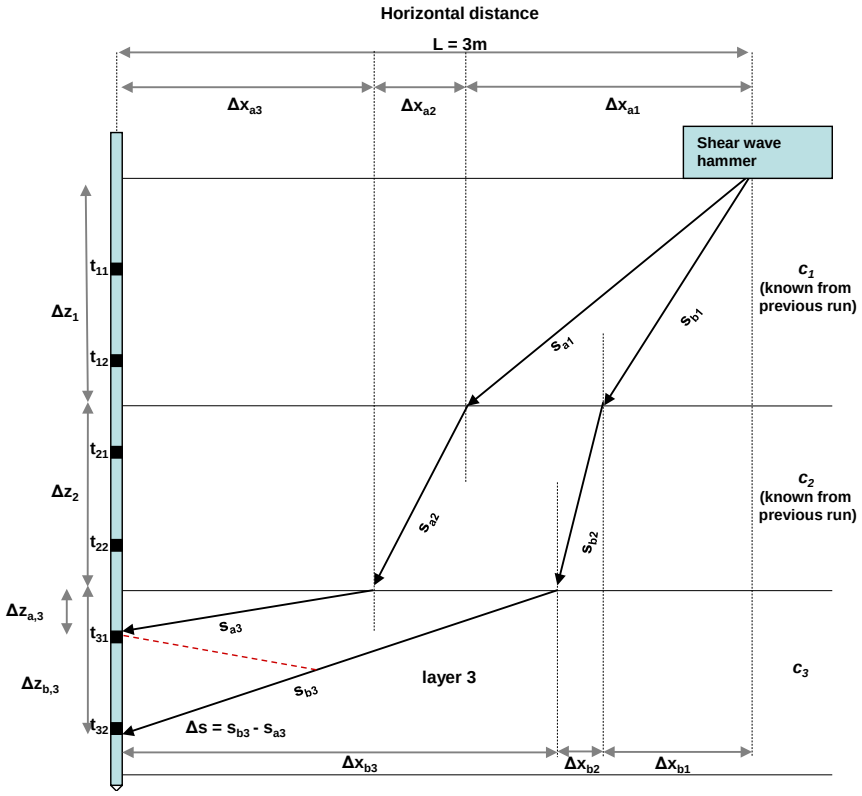

Figure 4: Schematic view of the minimization problem that was used to find the shear-wave velocity, c_n. An example is given for layer number $n = 3$. Through Snell's law, $4n + 1$ geometric relations can be formulated to find an optimized solution for the $4n + 1$ variables. The variables are explained in the text.

$$\begin{aligned}
\frac{\Delta x_{ai}}{s_{ai}\ c_i} &= \frac{\Delta x_{a(i+1)}}{s_{a(i+1)}\ c_{i+1}}, \\
\frac{\Delta x_{bi}}{s_{bi}\ c_i} &= \frac{\Delta x_{b(i+1)}}{s_{b(i+1)}\ c_{i+1}},\ i = 1..n-1,
\end{aligned} \tag{1}$$

$$\begin{aligned}
s_{ai} &= \sqrt{(\Delta x_{ai})^2 + (\Delta z_i)^2}, \\
s_{bi} &= \sqrt{(\Delta x_{bi})^2 + (\Delta z_i)^2}, \\
s_{an} &= \sqrt{(\Delta x_{an})^2 + (\Delta z_{an})^2}, \\
s_{bn} &= \sqrt{(\Delta x_{bn})^2 + (\Delta z_{bn})^2},
\end{aligned} \tag{2}$$

$$\begin{aligned}
\sum_{j=1}^{n} \Delta x_{aj} &= L, \\
\sum_{j=1}^{n} \Delta x_{bj} &= L, \\
c_n &= \frac{\mathrm{s}_{bn} - \mathrm{s}_{an}}{t_{n2} - t_{n1} - \sum_{i=1}^{n-1} \frac{\mathrm{s}_{bi} - \mathrm{s}_{ai}}{c_i}}.
\end{aligned} \tag{3}$$

Here s_{an} is the wave path belonging to the upper ray, and s_{bn} to the lower ray in target layer n. $\Delta x_{an,bn}$ are the horizontal components of the wave path, and Δz_n the vertical component. t_{n1} and t_{n2} are the arrival times at respectively the upper and lower geophone in the last (target) layer n. In these equations, i is the index for the layers above the target layer for which the shear-wave velocity is inverted. The amount of variables and equations to be solved equals $4n{+}1$;

s_{ai}, s_{bi}, Δx_{ai}, Δx_{bi} $(4n)$ and c_n (1). As the shear-wave velocities in the layers are sequentially solved, c_1 and c_2 are assumed known in the example of Figure 4.

Matlab's gradient-based "fmincon" function was used for setting up this non-
205 linear optimization, and within this function, the "Sequantial Quadratic Programming" (SQP) algorithm appeared most appropriate for this problem. Being a medium-scale algorithm, it stores full (dense) matrices, remaining stable for deeper layers. The amount of equations and variables in this problem is small enough for sufficient computational speed. Furthermore, the algorithm
210 was found to be insensitive of the initial guess. The shear-wave velocity was constraint in between 1 and 1000 m/s. Confidence in finding the global minimum can be reached by visual inspection of the objective function for the first layers.

215 The found shear-wave velocities are depicted in Figure 5. As discussed in Section 2.1, different choices can be made in defining the interval times, and these choices influence the computed shear-wave velocity profile. Computing the profile using cross correlation only, renders the solid grey profile with "+" markers. This profile is included to assess the effect of neglecting any near-field effects
220 and relying on "automatic" processing. The solid black line with "$\circ$" markers in

Figure 5 is the profile linked to choosing a combination of using the S-transform for the first layer, "peak picking" for the second layer and cross correlation for the rest of the layers; it is named "Combination 1" and is the resulting profile from the "Combination" profile in Figure 2. The only difference between the black and grey profiles is thus the adopted interval time for the first 2 meters. We can see that this difference has a relatively large influence on the first 15m of the profile. As discussed, the definition of interval time can be uncertain. The black profile (combination) seems more realistic, but the "true" profile probably lies somewhere between the black and grey profiles. Therefore, these "black" and "grey" profiles will be used for further analyses in this paper.

As extra information, the grey dotted "$*$" line is also plotted. This profile shows the effect of also choosing a peak-picked interval timing for the first layer, which, as can be seen, clearly has a minor effect. As a reference, the profile computed by the geotechnical service company that performed the SCPTs is given by the grey dotted "$\bullet$" line. This profile was computed assuming straight rays from source to geophone (so ignoring the wave refraction), and without taking the wave velocities of previously calculated shallower layers into account.

Next to the velocity profile in Figure 5, the laboratory soil classification is given, which is based on borehole samples taken at the same location. It can be seen that the weaker soil layers between approximately 15m and 23m depth are quite well reflected in the estimated velocities. The velocity jumps within this region can be caused by the thin stiffer layers within the softer layers (as depicted in the laboratory classification). As further comparison with geotechnical measurements, also the cone-tip resistance q_c and sleeve friction f_s of a CPT measurement at the same location are plotted together with the shear-wave velocity profile of Combination 1 in Figure 6. In this figure, we can see that in general the agreement in stiffness indication is quite reasonable; the CPT parameters also indicate the presence of a weaker layer between 15m and 23m depth. Within this weaker layer, a thin stiffer layer is present (at around 18m depth) which is reflected in both CPT output and the shear-wave velocity profile. Finally, a stiffer sand layer is present beyond 23m, at which depth the shear-wave velocity also increases.

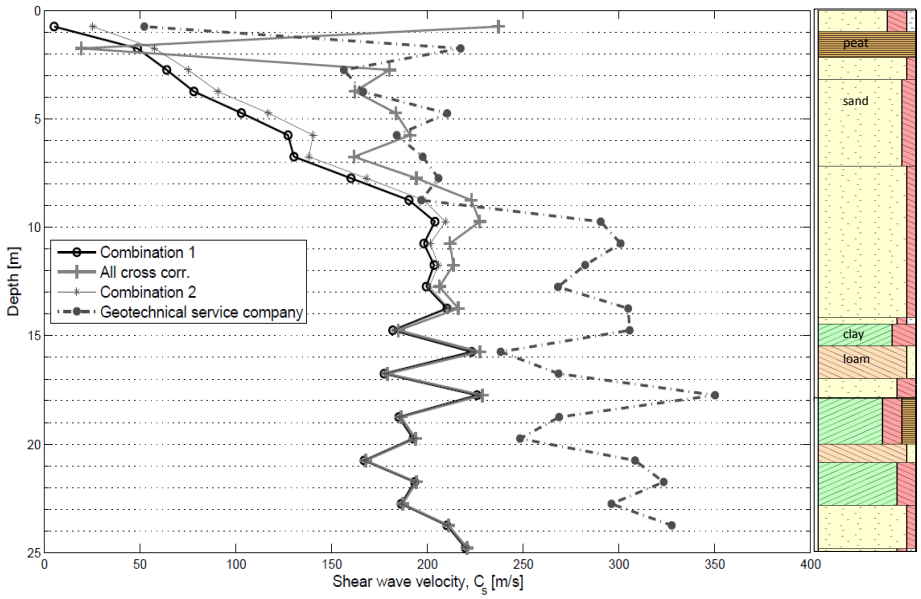

Figure 5: Derived shear-wave velocity profiles. The solid black "○" profile (Combination 1) is deemed most realistic; it is based on a combination of techniques to compute the interval time (see Figure 2) using cross-correlation for all layers, except the S-transform for the first layer and peak-picking for the second (because of near-field effects). The dotted grey "∗" profile (Combination 2) shows the effect of also taking a peak-picked interval time for the first layer. The solid grey "+" profile is based on using only cross-correlation. The dotted grey "•" profile was obtained by the geotechnical service company, using the "straight-ray" assumption.

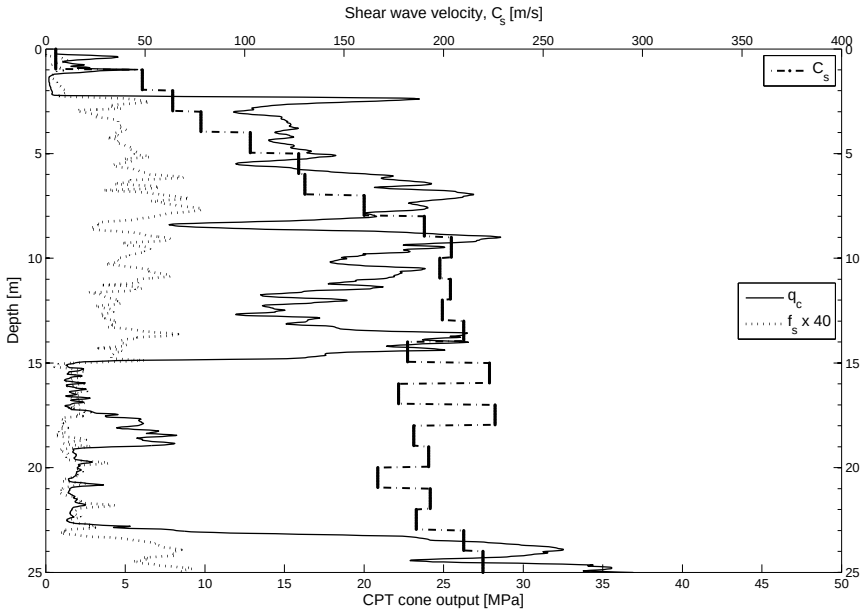

Figure 6: The derived shear-wave velocity profile of Combination 1 of Figure 5 in comparison to CPT output profiles measured at the same location. Note that the sleeve friction pressure f_s is multiplied by 40 in order to share the same value along the horizontal axis as the cone-tip resistance q_c.

2.3. Soil parameterisation

The in-situ saturated soil densities ρ and the internal angle of friction ϕ used and presented in this paper, are the design values for the near-shore wind farm. The values were determined by the geotechnical service company. For the in-situ density the relation of Robertson [22] was used. This relation is based on the cone tip and frictional resistance measured by the SCPT:

$$\rho/\rho_w = 0.27\log(R_f) + 0.36\log(q_t/p_a) + 1.236 \tag{4}$$

In this equation, q_t is the corrected cone resistance, R_f is the friction ratio between the sleeve friction and the corrected cone resistance, ρ_w is the mass

density of water and p_a is the atmospheric pressure. This in-situ soil density is used in this paper as input to the 3D elastic continuum model (Section 3).

The internal angle of friction ϕ was determined according to the relation between the initial modulus of subgrade reaction k, the relative density and internal angle of friction for different sand types, as depicted in the standards [2]. The obtained values were verified with triaxial tests. In this paper, the internal angle of friction serves merely as a reference for the stiffness of the soil. The in-situ density and the internal angle of friction profiles are shown in Figure 7. The relatively high values for the density and internal angle of friction in this figure indicate that this is quite a stiff soil profile.

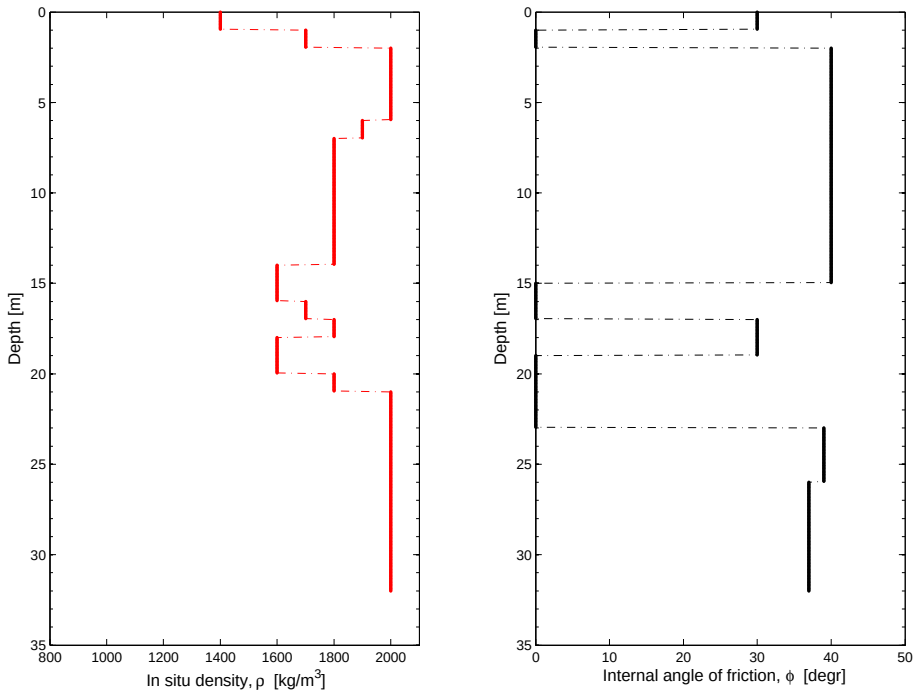

Figure 7: Profiles of in-situ density, ρ (left panel), and angle of internal friction for sand, ϕ (right panel). For peat and clay layers, ϕ is set to 0.

The estimation of the effective Poisson's ratio ν is a challenging task, as it is dependent on the type of soil, but for instance also on the occurring strain [23], the degree of water saturation and the loading frequency. In civil engineering practice, the Poisson's ratio is often taken as 0.3 for sand and 0.45 for cohesive material [24]. The small-strain Poisson's ratio can also be estimated from identified pressure-wave and shear-wave velocities. Measurement data acquired with a different cone at the same location, indicated much higher Poisson's ratios for this (saturated) sand [25]. In this data, we could extract both the pressure and the shear-wave velocities. With the ratio of these velocities and the in-situ porosity estimated from lab tests, the Poisson's ratio can be approximated using an effective two-phase model for wave propagation in a three-phase medium where the pore fluid contains minor gas bubbles (low-frequency limit [26], [27]).

In this theory, the Poisson's ratio is calculated by

$$\nu = \frac{3K_b - 2G}{2(3K_b + G)} \tag{5}$$

in which the bulk modulus K_b is calculated based on an effective fluid bulk modulus $K_{f,eff}$ as

$$K_b = H - \frac{4}{3}G - \frac{K_{f,eff}}{\Phi} \tag{6}$$

Here H is the Gasmann modulus as extracted from the pressure-wave velocity, and Φ is the porosity of the soil, in which the grains are assumed to be incompressible [26]. Then the degree of water and gas saturation (s_f and s_g respectively) are incorporated in $K_{f,eff}$ as

$$\frac{1}{K_{f,eff}} = \frac{s_f}{K_f} + \frac{s_g}{K_g} \tag{7}$$

in which $s_f = 1 - s_g$.

Similarly high Poisson's ratios for marine sediments were also observed by Hamilton [28], [29]. The higher apparent Poisson's ratio is related to the drainage capacity of the sand. Reference [30] addresses the relation between the drainage capacity of the soil, the permeability of the soil and the frequency of oscillation of the structure. The question whether the soil behaves drained or undrained during the vibrations of the installed MP does not belong to the scope of this paper; however, the higher Poisson's ratio can be considered for soil stiffness calculations. We will investigate 3 options, namely the Poisson's ratios of the "engineering practice", the profile found with the effective two-

phase medium theory, and an intermediate one (i.e., the average of these two). These 3 profiles are shown in Figure 8.

2.4. Stiffness range

Since we now have estimates of the shear-wave velocity, the density and the Poisson's ratio, we can calculate the Young's modulus E and shear modulus G of the soil profile. This can be done with the following relation:

$$c = \sqrt{\frac{E}{2(1+\nu)\rho}} = \sqrt{\frac{G}{\rho}}, \tag{8}$$

in which c is the shear-wave velocity. Due to the uncertainty in both Poisson's ratio and the interval time definition, we investigate the impact of these uncertainties by defining 3 "stiffness" cases. For the first - lowest stiffness - case, the solid black line profile in Figure 5 is used, in combination with the "engineering practice" Poisson's ratio. Then, for case 2, the same shear-wave velocity profile is chosen as in case 1 (black line), but combined with the intermediate Poisson's ratio. This higher Poisson's ratio causes case 2 to be stiffer than case 1. Then, the Young's modulus of case 3 is calculated by combining the solid grey velocity profile in Figure 5 (based on cross correlation only) and the Poisson's ratio determined with the effective two-phase medium theory. Case 3 is therefore an upper stiffness case. An overview of the cases is given in Table 1.

	CASE 1	**CASE 2**	**CASE 3**
dT method	Combination	Combination	Pure cross correlation
Poisson's ratio	Engineering practice	Average	Effective medium

Table 1: Overview of the considered soil stiffness profiles. The "Combination" is the profile for which the interval time (dT) for the first layer was determined with the S-transform, the second by peak-picking, and the rest by cross correlation (Figure 2). The Poisson's ratio profiles of the three cases can be found in Figure 8.

The Young's moduli profiles corresponding to the 3 cases are shown in Figure 9. In calculating these Young's moduli, the same density profile was used for all cases (shown in the left panel of Figure 7). We can see that the Young's modulus of case 1 is almost equal to that of case 2, as this difference is only caused by the different values of Poisson's ratio. In Section 3.2, we will see the associated difference in terms of pile deflections.

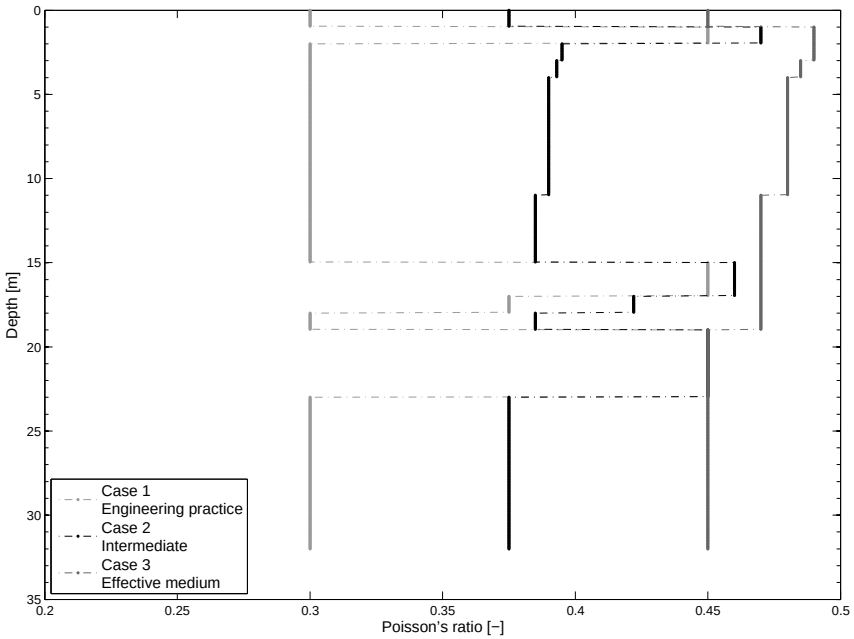

Figure 8: Profiles of the different Poisson's ratios for the 3 stiffness cases.

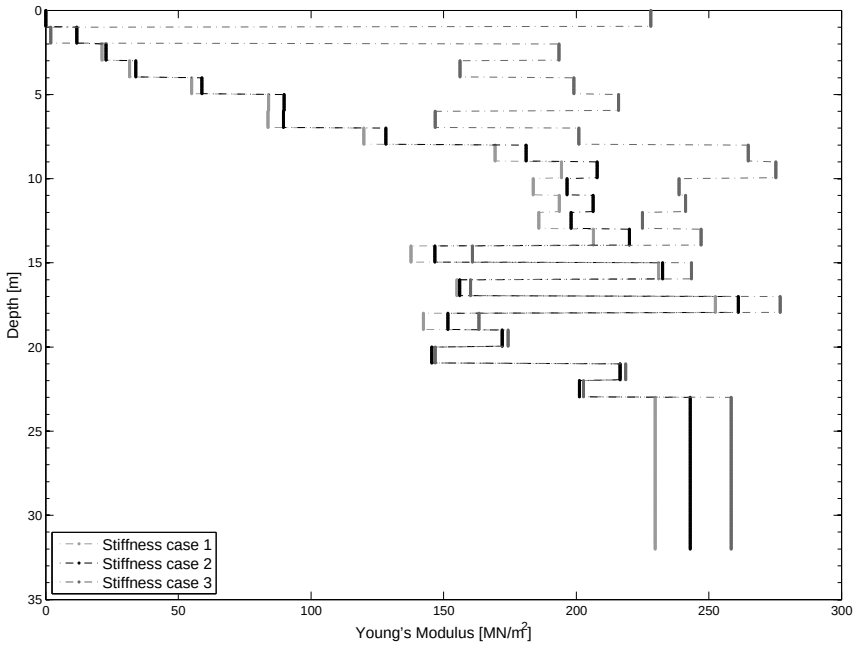

Figure 9: Profiles of the Young's moduli for the 3 stiffness cases.

2.5. Reference values

Empirical relations between shear modulus (in geotechnics often referred to as G_{max} or G_0) and CPT-output parameters are widely available. The weakness in such relations is that they aim to link local large-strain output of a CPT-cone with the larger scale small-strain characteristics of the soil needed for our analyses. Perhaps for that reason, these relations are often concluded to be site-specific, and coefficients in the relations are then tuned to provide a good match. Nevertheless, we check the applicability of such a relation for the data at hand. We compare the outcome with the shear modulus profile of case 2. An often used relation for sand developed by Seed and Idriss [31] is

$$G = 220 K_{2,max} (\sigma'_m)^{\alpha}. \tag{9}$$

In this equation, the coefficient $K_{2,max}$ is a function of the relative density D_r or void ratio e, α is a coefficient for the stress (depth) dependency of G and has a value of 0.5 according to the developers, and σ'_m is the mean effective confining pressure. This pressure is related to the vertical and horizontal effective stress by $\sigma'_m = (\sigma'_v + 2\sigma'_h)/3 = \sigma'_v(1 + 2K'_0)/3$. In this equation, K_0 is the coefficient of effective earth stress at rest: $K_0 \approx 1 - \sin(\phi)$, with ϕ the internal angle of friction. Paoletti et al. [32] also emphasized the site-specific character of this relation of Seed and Idriss (Equation (9)), and found α to be equal to 0.63 for offshore sands in the Adriatic Sea. Figure 10 compares the empirical relation (for α equal to 0.50: grey dotted line) and the shear moduli of case 2: black solid line.

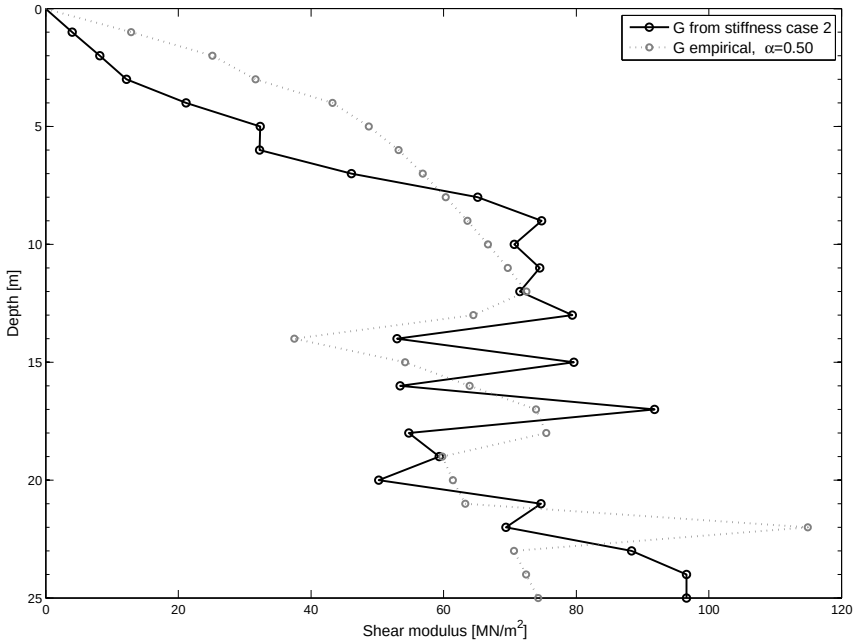

Figure 10: Comparison of identified shear modulus related to case 2 (black solid line) and reference empirical relation according to Equation (9) [31], with $\alpha = 0.50$ (grey dotted line).

Similar relations as equation (9) are available specifically for clay; however, because of the limited presence of clay at this site, they have not been included in Figure 10. We observe that the empirical relation predicts a higher shear modulus for the first shallow layers. This is most likely caused by the relatively high internal angle of friction of these layers. The profile of case 2 is conservative in this respect, because a high stiffness in these shallow layers will turn out to have a large influence on the pile deflections and the natural frequency. The empirical values are quite sensitive to the α parameter. Using an α equal to

0.63 as suggested by Paoletti et al. [32], would yield a factor 3 to 4 higher shear moduli for the deepest two-thirds of the layers. This confirms that designers must be cautious when using such empirical relations.

3. Modeling of pile deflections

To capture the true interaction mechanisms between pile and soil, a pile must be modeled as embedded in a 3D continuum. Only in such a model we can describe the soil reaction with the real material properties as identified in the previous section. This direct approach has a clear advantage over direct use of semi-empirical 1D models.

3.1. Model description

A linear elastic FE model was developed using ANSYS software, meshing the pile with shell elements, and the soil with solid elements. The pile has a diameter of 5m, embedded length of 32m and a wall thickness of 60mm. The soil stratum was given a vertical dimension of 50m, and a radius of 40 times the pile radius (i.e., 100m). A pile element size and soil element size of 0.25m was used close to the pile, and a combination of free and mapped meshing was applied. These model dimensions and mesh were verified to have converged; using smaller element sizes or increasing the size of the soil domain had negligible effect. Taking advantage

of the symmetry of the problem, only half of the circular pile and soil domain was modeled in order to decrease the computational effort. The soil elements within and outside the pile are attached to the pile elements; i.e. no slip is allowed between the pile and the soil. To simulate a shape of the pile that corresponds to the expected shape of the loaded MP, an overturning moment of 90Nm and horizontal force of 1N were applied at mudline by extending the pile with a 90m tower above mudline, at the top of which a horizontal force of 1N was applied. This moment-force ratio was retrieved from the design loads calculated for this wind farm, and it was found that this load eccentricity applies for most wind speeds. The wave and wind loading for this wind farm are expected to have the same direction. Obviously, the magnitude of this loading (90Nm/1N) is not representative, however, since we use a linear elastic model, the magnitude of the loading does not matter (as opposed to the moment-shear force ratio). The soil was assumed to consist of horizontally homogeneous, 1m thick, elastic layers and each layer was assigned the material properties derived for the different cases as described in Section 2. Because of the limited depth reached by the SCPT, the deepest 7m along the pile until the lower boundary of the model (from 25 to 50m depth) was assumed to be one homogeneous layer with the same properties as the layer above it (24 to 25m). Geotechnical data indicates that a quite uniform sand layer is indeed present at this depth. However, the

assumption of constant Young's modulus can be considered conservative, as it could be higher due to a larger effective overburden pressure.

3.2. Deflection shapes

Figure 11 displays the computed 3D pile deflection shapes for the three cases specified in Table 1. These lines represent the horizontal displacement (x-direction in Figure 12) of the nodes of the shell which are, in the undeformed situation, located on the plane (y-z plane, Figure 12) perpendicular to the plane of the applied loading (x-z plane, Figure 12). Figure 11 also includes the deflection shape of a 1D beam on Winkler foundation, of which the stiffness equals the initial stiffness of the p-y curves that were determined according to the design code [2], and subsequently used in the design model.

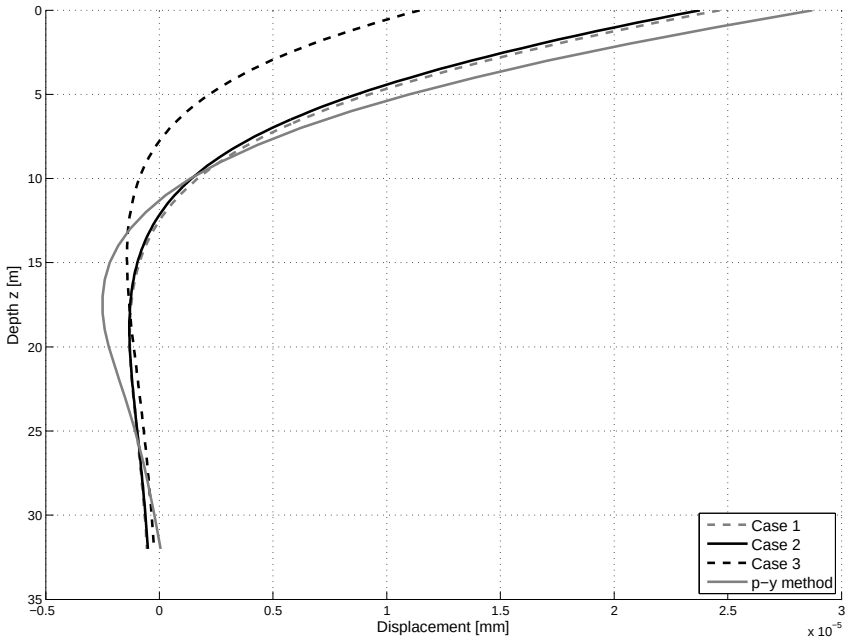

Figure 11: Comparison of pile displacements. The grey dashed line is the displacement of stiffness case 1, which is very similar to case 2 (black solid line). The black dashed line is stiffness case 3 (highest stiffness), and the grey solid line is the deflection computed using the *p-y* method.

It can be observed that the *p-y* curve approach seems to be conservative (i.e. yielding the largest displacements) in estimating the displacements when compared to all 3 stiffness cases which were calculated with the 3D FE model. In addition, more bending is present in the region between 10m and 25m depth in the pile deflection calculated with the *p-y* curve approach as opposed to the 3D FE results. The deflection at mudline of case 2 is 17% smaller than that predicted by the *p-y* curve method. Two factors may be responsible for this. First,

the input for the FE model was derived from seismic measurements, which are more appropriate for determining the small-strain shear modulus. Second, the FE model incorporates 3D phenomena for soil resistance to the large diameter piles. These phenomena can, for instance, include a large base shear at the pile tip [20] or pressure redistribution in the soil due to the Poisson's effect. Further, as expected, we see that there is little difference in the deflection shapes of cases 1 and 2. However, it is still interesting to see the influence of the estimated Poisson's ratio on the deflection shape, as this is the only parameter that varies between these cases (obviously, due to equation (8), the associated Young's modulus also changes slightly; see Figure 9). The higher Poisson's ratio for case 2 with respect to case 1 (see Figure 8) yields a 3.5% smaller deflection at mudline. As both cases have Poisson's ratio profiles that are still well below the incompressibility limit of 0.5, their relative difference does not yield a very large difference in stiffness. Nevertheless, we conclude that the shear modulus has the dominant influence on the deflection. More extensive sensitivity studies of the elastic parameters of soil on the response of the MP can also be found in [33] and [34]. As case 2 is based on the soil profiles which are deemed most realistic (see Sections 2.2 to 2.4), we will only consider this case in the remainder of this paper.

4. Effective 1D model

Currently, time-domain simulations of 10 min duration are used to assess the different load cases for the design lifetime of an OWT. The number of these simulations can reach up to 10,000 per design location and iteration. Given the fact that an average design effort for a wind farm comprises 2-3 locations with 3 iterations each, it is clear that the models should be computationally efficient. Now, in order to use the results of the more advanced 3D models, we need to tune the simpler engineering models used for design purposes. For the simpler model we choose the often preferred model of the engineering community: the beam on Winkler foundation. Such a distributed foundation model yields direct representation of the soil reaction, and the coupling between the lateral and rotational degrees of freedom at the mudline are automatically incorporated. Furthermore, the Winkler based substructure is extendable to include non-linear reaction mechanisms. In [17] we showed that, in trying to translate the 3D response to a 1D stiffness, simply dividing local forces by the collocated displacements leads to physically meaningless negative stiffness and singularities at certain locations. In order to avoid dealing with such not physical anomalies, we need to find a way to identify a positive definite 1D stiffness profile that yields nearly the same pile displacement as predicted by the 3D model. A

1D effective stiffness profile (i.e., $k_s(z)$ or $k_{s,0}(z)$ in the *p-y* curve method) is a soil-structure interaction functional parameter, capturing the geometry, the shape and material properties of both the pile and the soil. That explains why a one-to-one relation of the stiffness of a continuum (Young's and shear modulus) and a 1D Winkler foundation cannot be found.

4.1. Translation method

To find the 1D effective (*p-y* curve initial) stiffness, $k_s(z)$, we propose to optimize this stiffness profile in the engineering model to match both the deflection $u(z)$ and rotation $\psi(z)$ shapes obtained from the more advanced model. Note that we constrain ourselves by only assuming translational springs in the model, as this is often done in design practice. However, as 3D effects can be quite complex, it might, for instance, be reasonable to also introduce rotational springs in the 1D model.

The translation is accomplished by considering integrals of the equilibrium equation of a beam resting on a Winkler foundation, with $u(z)$ and $\psi(z)$ as the "known" 3D response and with $k_s(z)$ as the unknown stiffness of the distributed springs. First, the 3D nodal solutions need to be translated into a 1D target solution (line). As previously mentioned, for the horizontal displacement

line $u(z)$, the horizontal displacement is taken of the nodes of the shell which are, in the undeformed situation, located on the plane (y-z plane in Figure 12) perpendicular to the plane of the applied loading (x-z plane, Figure 12). For the 1D-target rotational shape $\psi(z)$, the difference in vertical displacements of the two nodes on the loading plane (x-z plane in Figure 12) were divided by the diameter of the pile. Such numerically computed profiles are not necessarily smooth enough for triple or double differentiation. Especially at the boundaries of the pile this can be an issue. To maintain a smooth shape also for the higher derivatives, the numerical values were fitted by polynomial functions. A piece-wise fit was applied, subsequently averaging overlapping parts of the fits of these pieces and refitting a single polynomial through the different piece-wise-averaged fits. For the deflections, the shape was split up in 3 parts, with 2 smaller parts focussing on the tip region of the pile. The same split was applied for the rotational shape, however, it was found that an extra split near the mudline (yielding a fourth part focussing on the top of the pile) gave a better overall fit.

We use the Timoshenko beam theory as the basis for the analysis. It was found that the shearing contributions to the rotations, which is included in this theory (as opposed to the Euler-Bernoulli theory), had to be included in order

to better match the 3D response of this relatively rigid, large diameter pile.

455 The equilibrium equations of a Timoshenko beam, representative for a monopile without external distributed forcing read:

$$GA\kappa(\frac{d^2u(z)}{dz^2} - \frac{d\psi(z)}{dz}) - k_s(z)u = 0, \tag{10}$$

$$GA\kappa(\frac{du(z)}{dz} - \psi(z)) + EI\frac{d^2\psi(z)}{dz^2} = 0, \tag{11}$$

where E and G are respectively the Young's and shear modulus of steel, I the second moment of area of the cross section of the pile, A the area of the cross section of the pile and κ the cross section-dependent Timoshenko shearing coefficient. For the shape of the cylindrical cross section of the pile, we used a value of $\kappa = 0.5$. For the purpose of this paper, it is more convenient to rewrite these equilibrium equations into a single equation. This can be done by differentiating equation (11) yielding

$$GA\kappa(\frac{d^2u(z)}{dz^2} - \frac{d\psi(z)}{dz}) + EI\frac{d^3\psi(z)}{dz^3} = 0, \tag{12}$$

and differentiating equation (10) twice to obtain

$$\frac{d^3\psi(z)}{dz^3} = -\frac{1}{GA\kappa}\frac{d^2(k_s(z)u(z))}{dz^2} + \frac{d^4u(z)}{dz^4}. \tag{13}$$

Replacing the first term in equation (12) by $k_s(z)u$ in accordance with equation (10), and substituting equation (13) into the second term of equation (12) yields a single equilibrium equation:

$$EI\frac{d^4u(z)}{dz^4} + k_s(z)u - \frac{EI}{GA\kappa}\frac{d^2(k_s(z)u(z))}{dz^2} = 0, \tag{14}$$

which is similar to the Euler-Bernoulli equilibrium relation, but it includes a third term to account for the shearing effect.

The boundary conditions for the case that we consider are

$$GA\kappa\Big(\frac{du}{dz}\Big|_{z=0} - \psi(0)\Big) = -F, \tag{15}$$

$$EI\frac{d\psi}{dz}\Big|_{z=0} = m, \tag{16}$$

$$GA\kappa\Big(\frac{du}{dz}\Big|_{z=L} - \psi(L)\Big) = 0, \tag{17}$$

$$EI\frac{d\psi}{dz}\Big|_{z=L} = 0, \tag{18}$$

in which F and m are the equivalent lateral force and overturning moment as applied in the 3D model. Note that this, in the case of simulating only half of the symmetric problem in the 3D model, implies that a factor of 2 has to be applied to the loading in the 1D model. The assumed boundary conditions as stated in equations (15) to (18) for a "free-free" 1D beam can be checked to hold for the 3D solution. When doing so, we find that indeed - due to 3D effects - these force and moment equilibria do not entirely apply for the 3D responses at these locations. Therefore, we could argue that this requires the introduction of discrete lateral and rotational springs at the tip as well as at the top of the pile, in order to - in the 1D model - reach force and moment equilibria at the boundaries. However, in the example case of this paper we will not apply any discrete springs at the boundaries, as an effective distributed stiffness can be found that can adequately capture the 3D response without the application of extra discrete springs. The sign convention of the 1D model is given in Figure 12.

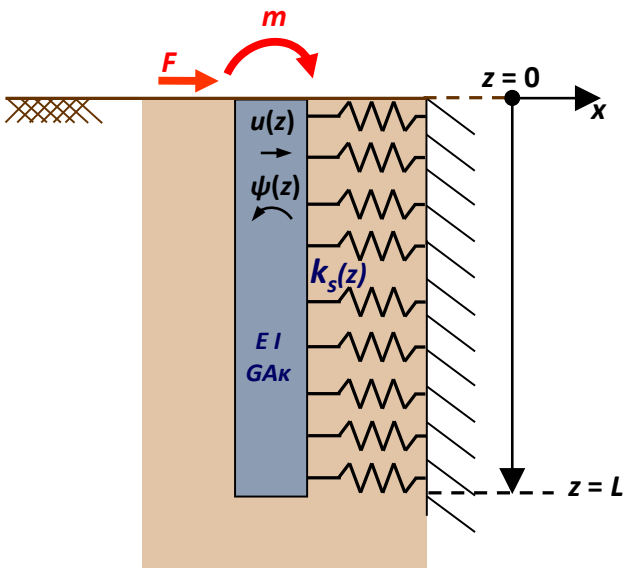

Figure 12: Graphical representation of the 1D beam model and the used sign convention.

In order to find the effective 1D stiffness $k_s(z)$, we assume a certain continuous parameterized function. We are only interested in physically realistic solutions, we do not allow negative stiffness in the resulting stiffness profile. We found that looking for a solution for $k_s(z)$ in the form of a fourth order polynomial suffices to capture the 3D effects. So, we assume

$$k_s(z) = p_0 + p_1 z + p_2 z^2 + p_3 z^3 + p_4 z^4, \tag{19}$$

which has 5 unknown constants. To find these 5 constants, we also formulate 5 equations, which are integrals of the force equilibrium equation (14).

For the first integral, we want the global force balance to hold over the full

length of the pile. Taking the integral of the equilibrium equation gives:

$$EI\frac{d^3u}{dz^3}\bigg|_{z_f^{(1)}}^{z_f^{(2)}} + \int_{z_f^{(1)}}^{z_f^{(2)}} k_s(z)u(z)dz \\ - \frac{EI}{GA\kappa}\Big(\frac{dk_s(z)}{dz}u(z) + k_s(z)\frac{du(z)}{dz}\Big)\bigg|_{z_f^{(1)}}^{z_f^{(2)}} = 0, \quad (20)$$

in which $z_f^{(1)}$ and $z_f^{(2)}$ are the integration boundaries ("$_f$": force; "(1)"/"(2)": lower/upper integration bound). As we want a force balance over the entire pile, for integral 1 $z_f^{(1)} = 0$ and $z_f^{(2)} = L$. We also want to match the global overturning moment. This can be achieved by multiplying equation (14) by z and again integrating over the beam length. Doing so, yields integral 2:

$$zEI\frac{d^3u}{dz^3}\bigg|_{z_m^{(1)}}^{z_m^{(2)}} - EI\frac{d^2u}{dz^2}\bigg|_{z_m^{(1)}}^{z_m^{(2)}} + \int_{z_m^{(1)}}^{z_m^{(2)}} zk_s(z)u(z)dz \\ - \frac{EI}{GA\kappa}\Big(z\Big(\frac{dk_s(z)}{dz}u(z) + k_s(z)\frac{du(z)}{dz}\Big) - k_s(z)u(z)\Big)\bigg|_{z_m^{(1)}}^{z_m^{(2)}} = 0. \quad (21)$$

For the global moment equilibrium integral 2, $z_m^{(1)} = 0$ and $z_m^{(2)} = L$ (subscript "m" stands for moment).

We now have 2 equations, so 3 more equations are needed to solve uniquely for the 5 unknowns. To establish these, we take the same integrals, but we now focus on equilibria of parts of the beam; a local force equilibrium and 2 local moment equilibria. As we do not yet know which parts of the beam we should focus on to get the best solution (match), we leave the integration limits unknown. We find the solution by sweeping the upper and lower limits of the integrals in steps ΔL and checking which combination gives the optimal $k_s(z)$.

The local "force" integral focuses on the upper part of the pile (by sweeping the integration limits $z_{f,t}^{(1)}$ and $z_{f,t}^{(2)}$ ("$_{f,t}$": force, top) from 0 to $L - \Delta L$). As for the "moment" integrals, one focuses on the upper and the other one focuses on the lower part of the pile (from L to $0 + \Delta L$). So, the third integral is given by equation (20), however, with integration limits that are swept starting from the top:

$$\begin{aligned} z_{f,t}^{(1)} &= 0 \;..\; \Delta L \;..\; (L - 2\Delta L), \\ z_{f,t}^{(2)} &= z_{f,t}^{(1)} + \Delta L \;..\; \Delta L \;..\; L - \Delta L. \end{aligned} \tag{22}$$

Similarly, the fourth integral, given by equation (21), focuses on the equilibrium of moments at the top of the pile by sweeping the integration limits:

$$\begin{aligned} z_{m,t}^{(1)} &= 0 \;..\; \Delta L \;..\; (L - 2\Delta L), \\ z_{m,t}^{(2)} &= z_{m,t}^{(1)} + \Delta L \;..\; \Delta L \;..\; L - \Delta L. \end{aligned} \tag{23}$$

Finally, the fifth integral, also given by equation (21), focuses on the equilibrium of moments at the bottom of the pile by sweeping the integration limits:

$$\begin{aligned} z_{m,b}^{(2)} &= L \;..\; -\Delta L \;..\; 2\Delta L, \\ z_{m,b}^{(1)} &= z_{m,b}^{(2)} - \Delta L \;..\; -\Delta L \;..\; \Delta L. \end{aligned} \tag{24}$$

So, in total 6 integration limits (3 local integrals with 2 integration limits each) are swept with steps of ΔL. Note that a linear system of equations is solved for each combination of the integration bounds, giving a unique solution for $k_s(z)$.

Of these solutions, only the positive definite stiffness profiles are considered for calculating the corresponding deflection and rotation shapes using the 1D Timoshenko model.

Subsequently, we judge the quality of the solutions and select the optimal one. Depending on the end-goal of the analysis, the definition of the optimum might differ. For instance, a full match in bending moment for all depths with respect to the 3D model might be preferred instead of exactly matching the displacement and rotation at mudline. In this paper, we assess the quality of the solution based on a the fit for the deflection u, the slope $\frac{du}{dz}$ (or u'), the rotation ψ and curvature ψ' of the 1D model with respect to those of the 3D model for all depths. Obviously, such a misfit function can be tailored to the purpose of the user. We define the "cost" of the fit as

$$C_{u,u',\psi,\psi'} = \frac{\sum_{i=0}^{i=L} \left|u_{1D,i} - u_{3D,i}\right|}{4\sum_{i=0}^{i=L} \left|u_{3D,i}\right|} + \frac{\sum_{i=0}^{i=L} \left|\frac{du_{1D}}{dz}|_i - \frac{du_{3D}}{dz}|_i\right|}{4\sum_{i=0}^{i=L} \left|\frac{du_{3D}}{dz}|_i\right|} + \frac{\sum_{i=0}^{i=L} \left|\psi_{1D,i} - \psi_{3D,i}\right|}{4\sum_{i=0}^{i=L} \left|\psi_{3D,i}\right|} + \frac{\sum_{i=0}^{i=L} \left|\frac{d\psi_{1D}}{dz}|_i - \frac{d\psi_{3D}}{dz}|_i\right|}{4\sum_{i=0}^{i=L} \left|\frac{d\psi_{3D}}{dz}|_i\right|}. \quad (25)$$

4.2. Translation Results

For case 2, we obtained satisfactory results by sweeping the 6 integration bounds with steps of $\Delta L = 2.13$m. Figure 13 shows the resulting 1D effective initial stiffness $k_s(z)$, which now incorporates 3D effects and true small-strain reaction properties. As a reference, the initial stiffness as determined with the *p-y* curve

method is also shown in the same figure. The resulting deflection, slope, rotation and curvature profiles and the fits with the corresponding 3D responses are given in Figures 14 and 15, respectively. In Figure 13, we see that a somewhat larger stiffness $k_s(z)$ is mobilized at the upper two-third part of the pile. The weaker soil layer between 13m and 20m depth is - due to a combination of relatively constant shear-wave velocity and 3D effects - not as dominantly present in the effective stiffness as in the *p-y* stiffness. We also note that at mudline $k_s(z)$ is not zero. The higher stiffness in the shallow region can reflect the phenomenon that was already mentioned in Sections 1 and 3: an underestimation of the shallow-depth stiffness. The stiffness of the upper layers of the soil profile has a dominant influence on the natural frequency of the structure. As a reference, the previously shown Young's profile of stiffness case 2 is plotted alongside the effective stiffness profile in Figure 13. We can see that the 3D and 1D stiffness profiles share some shape characteristics. However, we note that the 1D profile also captures the interaction with the structure, and thus should not necessarily follow the 3D continuum stiffness profile.

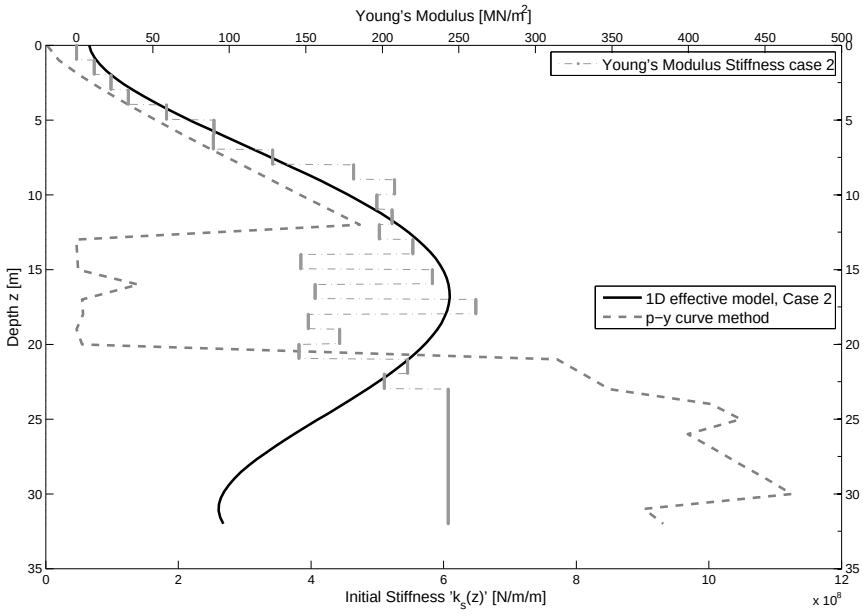

Figure 13: The effective $k_s(z)$ of stiffness case 2, found for a pile loaded with an overturning moment/horizontal force ratio of 90m at mudline (black solid line). This initial stiffness incorporates 3D modelling effects, and in-situ seismic small strain characterization of the soil. As a reference, the *p-y* curve initial stiffness is given by the grey dashed line. Also the Young's profile for stiffness case 2 which was input for the 3D model, is plotted as a reference (grey dashed-dotted line).

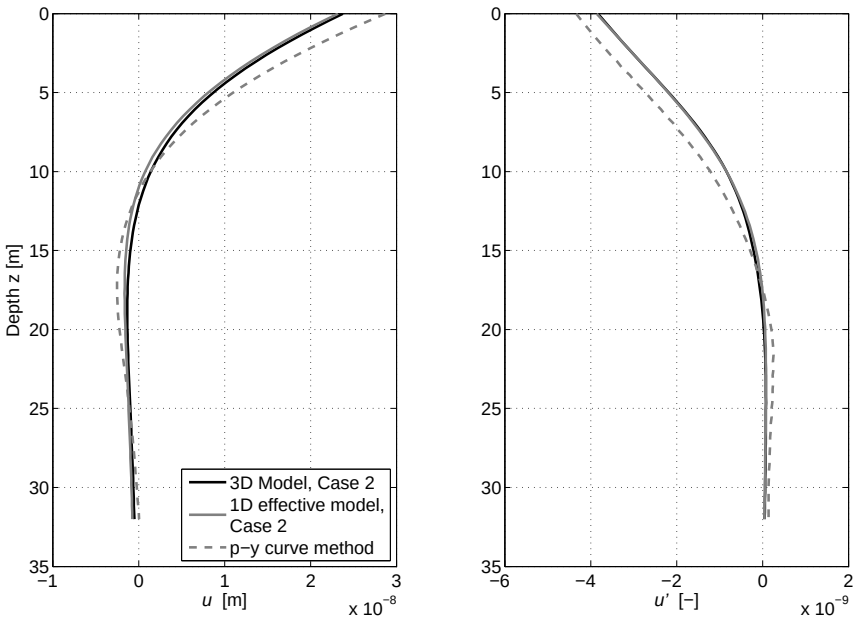

Figure 14: Deflection u (left panel) and slope u' (right panel) of a 1D Timoshenko beam with the found effective stiffness k_s given in Figure 13 caused by an overturning moment of 180Nm and 2N horizontal force at mudline (grey solid lines). The match with the 3D responses (black solid lines) is good. As a reference: the grey dashed lines are the deflection and slope of a Timoshenko beam with the initial stiffness derived from the *p-y* curve method (as also depicted in Figure 13).

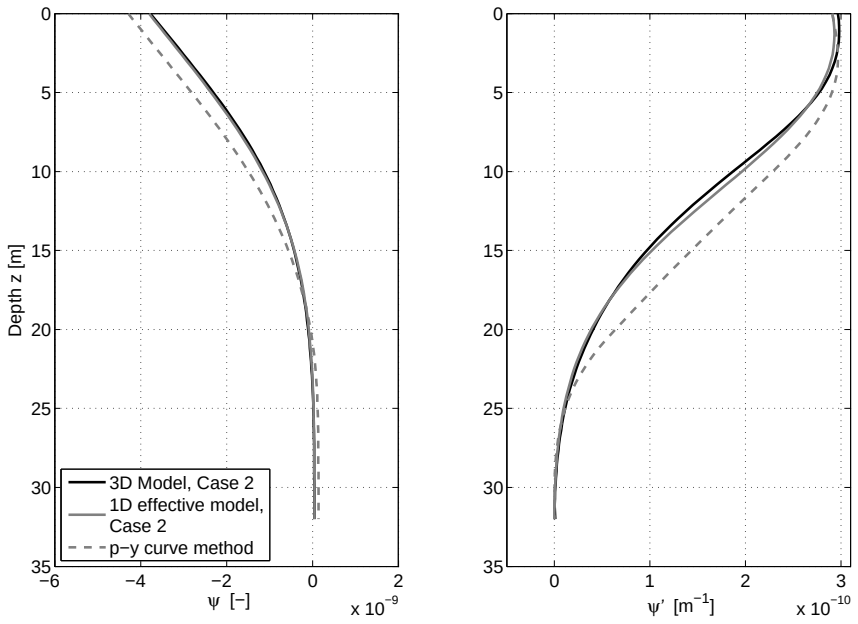

Figure 15: The rotations ψ (left panel) and curvature ψ' (right panel) associated with the deflection and slope profiles given in Figure 14: the 1D effective solutions (grey solid lines), the responses of the 3D model (black solid lines) and the responses derived with the *p-y* curve method (grey dashed line).

In Figure 14 we see, as in Figure 11, a stiffer response in the small-strain 3D model (and the 1D effective fits) compared to the *p-y* curve method. Also, the location of the maximum bending moment (reflected by the curvature ψ' plot in the right panel of Figure 15) as determined with the *p-y* curve method is located a couple of meters below that of the 3D model. This disparity is caused by the difference in shallow-layer stiffness between the methods (indicated also in Figure 13). The maximum bending moment of the 3D model is located just

below the mudline.

The values of the cost of the fits $C_{u,u',\psi,\psi'}$ and its separate components C_u, $C_{u'}$, C_ψ and $C_{\psi'}$ of case 2 are given in Table 2. To check the general applicability of this best solution (the effective $k_s(z)$) for other load cases, four other loading cases were simulated in the 3D model: a variation of around 10% in the effective lever arm of the loading for which the effective $k_s(z)$ was inverted, a ratio in the overturning moment m and horizontal force F of 100 and 80. In addition, two more radical differences were evaluated; an effective lever arm of 45 (50% of the original target-shape loading), and a moment-only case. The quality of the fits of the 1D model using the 1D stiffness profile as presented in Figure 13 with the 3D response of the other load cases was found to be equally satisfactory. As can be seen in Table 2, the cost values for these other load cases are comparable with the costs of the fit of the loading case for which the stiffness was identified.

	$C_{u,u',\psi,\psi'}$	C_u	$C_{u'}$	C_ψ	$C_{\psi'}$
Case 2 m/F=90m (target)	0.0454	0.0269	0.0057	0.0057	0.0072
m/F=100m	0.0445	0.0260	0.0056	0.0057	0.0071
m/F=80m	0.0466	0.0280	0.0057	0.0056	0.0072
m/F=45m	0.0538	0.0348	0.0061	0.0055	0.0075
m=1 Nm, F=0 N	0.0351	0.0165	0.0058	0.0060	0.0068

Table 2: Values of equation (25) for the best solution (the effective stiffness $k_s(z)$ which yields the lowest value for $C_{u+u'+\psi+\psi'}$) for stiffness case 2. This effective stiffness profile was tested to be compatible for 4 other load cases. The costs of the fits of the 1D response with the 3D response for these load cases are also included in this table.

From Table 2, we see that the cost of the fit of the displacement over the full length of the pile is 0.0269. This number can be multiplied by 4 to yield the percentage difference (see equation (25)): 10.76%. The overall rotations show a 2.28% difference, and the overall curvature (i.e. the correspondence in bending moment, see equation (16)) difference is 2.88%. Similar matching efforts (although including rotational springs along the pile and at its base) yielded a difference in static displacement at the top of the pile of 14.0%, and a difference in rotation at the same location of 8.7% [20]. If we also only consider the top of the pile, the mismatch in static deflection and rotation at this location is 2.40% and 0.88% respectively.

5. Resulting natural frequencies

Since we now have a 1D effective lateral stiffness, we can employ it in an aeroelastic model, and check the effect of the found stiffness profiles on the natural frequency of the entire system (support structure including rotor-nacelle assembly). This is done by performing an eigenfrequency analysis in the BHawC program, the aeroelastic code used by Siemens Wind Power. Table 3 lists the resulting frequencies obtained with the soil stiffness identified with the help of the p-y curve method, and those obtained by using the here presented seismic characterization and 3D modelling approach.

	Mode	Natural frequency [Hz]	Δ w.r.t. p-y curve method
p-y **curve**	**F-A**	0.288	-
	Si-Si	0.292	-
Case 2	**F-A**	0.291	+1.04 %
	Si-Si	0.295	+1.03 %
Clamped	**F-A**	0.308	+6.94 %
	Si-Si	0.313	+7.19 %

Table 3: Overview of natural frequencies of the fore-aft and side-side vibrational modes (first bending modes) of the entire OWT system for the different stiffness cases.

From Table 3, we can see that the proposed method results in a 1.04% (case 2) increase in natural frequency for the fore-aft bending mode of the structure. We have to note that such a relative increase is site-dependent; the impact of a certain SSI modelling approach on the natural frequency of the structure de-

pends on the relative stiffness of the soil profile. To assess this impact, an extra case is given in Table 3: clamping the foundation at mudline. This case yields the upper limit influence of the soil stiffness on the natural frequency of this OWT structure. From this we can conclude that the soil of the selected design location can be characterized as quite stiff: clamping the foundation increases the natural frequency with about 7% with respect to the *p-y* approach. This is confirmed by the geotechnical profile, consisting of mostly sand with an internal angle of friction ϕ of around 38 degrees (Figures 5 and 7).

As discussed, case 2 is thought to be most realistic, and was therefore used in presenting the translation method. Clearly the upper stiffness case 3 or even the shear-wave velocities supplied by the geotechnical service company (the grey dotted "•" line in Figure 5), would result in higher natural frequencies as found for the here presented case 2.

6. Conclusions

The fundamental natural frequencies of installed OWTs are generally higher than aimed for in design. This implies a waste of construction steel, which is often used to stiffen-up the support structure. The first natural frequency needs to be predicted with quite a high accuracy, as resonance regimes below and

above this frequency exist that can cause structural fatigue. The discrepancy in frequency is expected to be caused by an underestimation of the stiffness occurring in the interaction between soil and the large-diameter rigidly behaving OWT foundations. In the applied p-y curve design method, the modulus of subgrade reaction k was calibrated for flexible slender piles. It is this parameter that defines the initial stiffness, k_s, which in turn defines the modal response of the support structure. k_s is truly a SSI parameter, dependent on the geometry, shape and material properties of both the structure and the soil. Many studies have proposed other empiric, tunable relations for this parameter, with the conventional geotechnical parameters as input. These geotechnical parameters are measured in-situ using CPTs and borehole samples, which are both soil-disturbing, large-strain measurement techniques.

In this paper, we present two innovative steps for improved assessment of the initial stiffness of soil in contact with large diameter foundations. Firstly, as we are interested in the modal properties of the OWT, we need to assess the dynamic, small-strain soil reaction. This property is best captured by seismic measurements. The SCPT is a well-established technique measuring both local and more global properties of the soil-stratum. A geophysical method was

used to extract the shear modulus (G) of the soil layers. The estimated shear modulus G is input for a 3D SSI model, which is used to extract the proper small-strain pile responses.

Secondly, we present a translation method to find the initial stiffness $k_s(z)$, being a true SSI interaction parameter. It can be captured with prototype measurements, or, when these are not available, it can be approximated with a 3D model in which more realistic deformations of both soil and structure are taken into account (compared to 1D). Instead of trying to find a general tunable relation, we suggest developing such a 3D model for every design position and use the presented translation method to extract the 1D-effective initial stiffness. This Winkler foundation stiffness can then be used in the simpler and fast simulation models, to directly compute the occurring stresses in the monopile.

The steps were demonstrated for a design location in a near-shore wind farm, of which the soil profile can be characterized by mostly stiff dense sand, and a layer of stiff clay. The optimal 1D effective stiffness profile was defined as yielding a balanced fit: scoring well on deflection, slope, rotations and curvature. Obviously, such a misfit function can be tailored to the purpose of the user. The selected 1D stiffness profile gave a satisfactory good match in pile responses with

respect to the 3D model, resulting in a small mismatch in deflection u and rotation ψ at the mudline of 2.40% and 0.88% respectively. The overall mismatch (for all depths) of the deflections and rotations was 10.76% and 2.88%. The match in profiles of the slope u' and curvature ψ' was also found to be good, yielding similar values for the mismatch as the overall rotations. The optimal 1D-effective stiffness is a profile with a higher stiffness (as compared to the p-y approach) for the upper two-thirds of the soil layers. The quality of the fits obtained with the here presented method will depend on the soil profile and the geometry of the pile. For the presented case, a Winkler foundation with only lateral springs proved sufficient to match the 3D response. However, if the 3D global effect are not sufficiently captured by lateral springs only, more degrees of freedom can be added to the 1D model: for instance discrete springs at the boundary of the pile, or distributed rotational springs along its shaft.

The soil profile of the demonstrated design location is typical for many North Sea locations: rather stiff soil conditions with dense sand and a few thin layers of clay. When clamping the foundation at mudline, it was found that the upper limit of increase in the fundamental natural frequency of the complete structure (including tower and rotor-nacelle assembly) with respect to the initial stiffness

profile determined with the p-y curve method was only 7%. The here suggested stiffness, incorporating in-situ measured small-strain soil reactions and 3D global SSI effects, results in a 1.04% increase of the fundamental natural frequency. Obviously, many other mechanisms and aspects might also cause the described discrepancy between measured and modeled frequency. In any case, the method suggested here is believed to be an important step towards a more realistic assessment of the problem.

Acknowledgement

The authors would like to express their gratitude for the funding received from the Dutch government (project number TKIW02001), enabling the in-situ measurements and research we performed on Dynamic Soil-Structure Interaction: the DISSTINCT project.

7. References

[1] D. Kallehave, B. W. Byrne, C. L. Thilsted, K. K. Mikkelsen, Optimization of monopiles for offshore wind turbines, Philos Tr Roy S-A 373 (2035) (2015) 20140100.

[2] Offshore Standard DNV-OS-J101 Design of offshore wind turbine structures (October 2010).

[3] H. Matlock, Correlations for design of laterally loaded piles in soft clay, in: Offshore Technology in Civil Engineering: Hall of Fame Papers from the Early Years, ASCE, 1970, pp. 77–94.

[4] M. O'Neill, J. Murchinson, Fan evaluation of p-y relationships in sands, Tech. rep., A report to the American Petroleum Institute (1983).

[5] M. Damgaard, V. Zania, L. V. Andersen, L. B. Ibsen, Effects of soil–structure interaction on real time dynamic response of offshore wind turbines on monopiles, Eng Struct 75 (2014) 388–401.

[6] K. Terzaghi, Evaluation of coefficients of subgrade reaction, Géotechnique 5 (4) (1955) 297–326.

[7] S. Limkatanyu, K. Kuntiyawichai, E. Spacone, Response of reinforced concrete piles including soil–pile interaction effects, Eng Struct 31 (9) (2009) 1976–1986.

[8] S. Soerensen, L. Ibsen, A. Augustesen, Effects of diameter on initial stiffness of p-y curves for large-diameter piles in sand, numerical methods in geotechnical engineering, in: Proc. of the 7th European Conference, Trondheim/Norway, Vol. 2, 2010.

[9] J. Stevens, J. Audibert, et al., Re-examination of p-y curve formulations, in: Offshore Technology Conference, Offshore Technology Conference, 1979.

[10] D. Kallehave, C. L. Thilsted, M. Liingaard, Modification of the API p-y formulation of initial stiffness of sand, in: Offshore Site Investigation and Geotechnics: Integrated GeotechnologiesPresent and Future. Proceedings of the 7th International Conference on Offshore Site Investigations and Geotechnics, London, Society of Underwater Technology, 2012, pp. 465–472.

[11] P. Doherty, K. Gavin, Laterally loaded monopile design for offshore wind farms, Energy 165 (Issue EN1) (2012) 7–17.

[12] W. G. Versteijlen, A. V. Metrikine, J. S. Hoving, E. Smid, W. E. de Vries, Estimation of the vibration decrement of an offshore wind turbine support structure caused by its interaction with soil, in: Proceedings of the EWEA Offshore 2011 Conference, Amsterdam, The Netherlands, European Wind Energy Association, 2011.

[13] C. Leth, S. P. H. Sørensen, R. T. Klinkvort, A. Augustesen, O. Hededal, L. B. Ibsen, A snapshot of present research at AAU and DTU of large-diameter piles in coarse-grained materials, in: The Nordic Geotechnical Meeting, 2012, pp. 491–498.

[14] K. Abdel-Rahman, M. Achmus, Finite element modelling of horizontally loaded monopile foundations for offshore wind energy converters in germany, in: International Symposium on Frontiers in Offshore Geotechnics (ISFOG), Perth, Australia, Taylor & Francis London, 2005, pp. 309–396.

[15] K. Lesny, J. Wiemann, Finite-element-modelling of large diameter monopiles for offshore wind energy converters, in: Proceedings of the GeoCongress, Atlanta, Georgia, USA, 2006.

[16] K. Thieken, M. Achmus, K. Lemke, A new static p-y approach for piles with arbitrary dimensions in sand, Geotechnik 38 (4) (2015) 267–288. doi:http://dx.doi.org/10.1002/gete.201400036.

[17] W. G. Versteijlen, K. N. van Dalen, A. V. Metrikine, L. Hamre, Assessing the small-strain soil stiffness for offshore wind turbines based on in situ seismic measurements, in: J. Phys. Conf. Ser., Vol. 524, IOP Publishing, 2014, p. 012088. doi:10.1088/1742-6596/524/1/012088.

[18] S. A. Ashford, T. Juirnarongrit, Evaluation of pile diameter effect on initial modulus of subgrade reaction, J. Geotech. Geoenviron. Eng. 129 (2003) 234–242. doi:http://dx.doi.org/10.1061/(ASCE)1090-0241(2003)129:3(234).

[19] L. J. Prendergast, K. Gavin, P. Doherty, An investigation into the effect of scour on the natural frequency of an offshore wind turbine, Ocean Eng. 101 (2015) 1–11. doi:http://dx.doi.org/10.1016/j.oceaneng.2015.04.017.

[20] Varun, D. Assimaki, G. Gazetas, A simplified model for lateral response of large diameter caisson foundations - linear elastic formulation, Soil Dyn Earthq Eng 29 (2) (2009) 268–291.

[21] R. G. Stockwell, L. Mansinha, R. Lowe, Localization of the complex spectrum: the S-transform, IEEE T Signal Proces 44 (4) (1996) 998–1001.

[22] P. K. Robertson, K. Cabal, Estimating soil unit weight from CPT, in: 2nd International Symposium on Cone Penetration Testing, 2010, pp. 2–40.

[23] T. Kokusho, Cyclic triaxial test of dynamic soil properties for wide strain range, Soils Found. 20 (2) (1980) 45–60.

[24] J. E. Bowles, Foundation Analysis and Design, McGraw-Hill, New York, 1996.

[25] A. de Groot, Determination of dynamic soil properties from in-situ offshore low-frequency seismic measurements (2014).

[26] K. N. van Dalen, Multi-component Acoustic Characterization of Porous Media, Springer, 2013.

[27] J. J. M. Carcione, Wave fields in real media: Wave Propagation in Anisotropic, Anelastic, Porous and Electromagnetic Media, Vol. 38 of Handbook of Geophysical Exploration: Seismic Exploration, 2007.

[28] E. L. Hamilton, Elastic properties of marine sediments, J Geophys Res 76 (2) (1971) 579–604.

[29] E. L. Hamilton, Vp/Vs and Poisson's ratios in marine sediments and rocks, J Acoust Soc Am 66 (4) (1979) 1093–1101.

[30] M. Damgaard, M. Bayat, L. V. Andersen, L. B. Ibsen, Assessment of the dynamic behaviour of saturated soil subjected to cyclic loading from offshore monopile wind turbine foundations, Comput. Geotech. 61 (2014) 116–126.

[31] B. Seed, H., I. Idriss, Soil moduli and damping factors for dynamic response analysis, Tech. rep., Earthquake Engineering Research Centre, University of California, Berkeley, report No. EERC 70-10 (1970).

[32] L. Paoletti, Y. Hegazy, S. Monaco, R. Piva, Prediction of shear wave velocity for offshore sands using CPT data–Adriatic Sea, in: Proc. of 2nd International Symposium on Cone Penetration Testing (CPT10), Vol. 2, 2010, pp. 361–368.

[33] M. Damgaard, L. V. Andersen, L. B. Ibsen, Dynamic response sensitivity of an offshore wind turbine for varying subsoil conditions, Ocean Eng. 101 (2015) 227–234. doi:http://dx.doi.org/10.1016/j.oceaneng.2015.04.039.

[34] M. Damgaard, L. V. Andersen, L. B. Ibsen, H. S. Toft, J. D. Sørensen, A probabilistic analysis of the dynamic response of monopile foundations: Soil variability and its consequences, Probabilist. Eng. Mech. 41 (2015) 46–59. doi:http://dx.doi.org/10.1016/j.probengmech.2015.05.001.